


 Cite this: *RSC Adv.*, 2023, **13**, 24413

High stability and strong luminescence CsPbBr_3 – Cs_4PbBr_6 thin films for all-inorganic perovskite light-emitting diodes†

Tianxinyu Bai, Shenwei Wang, Kexin Zhang, Chunyang Chu, Yingqiang Sun and Lixin Yi*

All-inorganic lead halide perovskite, characterized by its exceptional optical and electrical properties, is burgeoning as a potential optoelectronic material. However, the standalone CsPbBr_3 component encounters several challenges including small exciton binding energy (≈ 40 meV) and long charge diffusion length, giving rise to low photo-luminescence quantum-yield (PLQY); ion migration leads to instability in device operation, hindering device operation and potential development. To circumvent these limitations, our research endeavors to construct a novel core–shell structure that transforms the continuous $[\text{PbX}_6]^{4-}$ octahedron into an isolated octahedral structure. We introduce the Cs_4PbBr_6 phase with 0D structure to passivate the vacancy defects in CsPbBr_3 , thereby suppressing ion migration and enhancing the luminescence intensity and stability. Our methodology involves fabricating dense CsPbBr_3 – Cs_4PbBr_6 composite films using a co-evaporation method, wherein the molar ratio of CsBr and PbBr_2 is precisely adjusted. The films are subsequently rapidly annealed under ambient air conditions, and the effects of different annealing temperatures and annealing times on the CsPbBr_3 – Cs_4PbBr_6 films were investigated. Our results demonstrate significantly improved stability of the annealed films, with a mere 15% decrease in PL intensity after 100 days of storage under ambient air conditions at 48% relative humidity (RH). Based on this thin film, we fabricated all-inorganic structure $\text{Ag}/\text{N–Si}/\text{CsPbBr}_3$ – $\text{Cs}_4\text{PbBr}_6/\text{NiO}/\text{ITO}$ light emitting diodes (LEDs), the devices have a low turn-on voltage $V_T \sim 3$ V and under unencapsulated, ambient air conditions, it can operate continuously for 12 hours under DC drive with only 10% attenuation. The results we obtained open up the possibility of designing and developing air-stable perovskite LEDs.

 Received 13th June 2023
 Accepted 4th August 2023

 DOI: 10.1039/d3ra03947a
rsc.li/rsc-advances

1. Introduction

Metal halide perovskites CsPbX_3 ($\text{X} = \text{Br}$, I , and Cl) have become a research hotspot in recent years due to their extraordinary optoelectronic properties,^{1,2} such as extremely narrow emission bandwidth³ (full-width at half-maximum ~ 20 nm), tunable bandgap,⁴ excellent charge-transport properties,⁵ these unique characteristics have been drawing great attention for high-performance perovskite-based devices, for instance light emitting diodes (LEDs),^{6–8} solar cells^{9–11} and photodetectors.¹² However, the high electron and hole mobility of 3D metal halide perovskites with low exciton binding energy leads to low photoluminescence quantum yield (PLQY) in the low excitation regime¹³ and low electroluminescence (EL) efficiency of the

devices. However, their poor stability to light, heat, air and humidity limits the applications.¹⁴

Many solutions have been proposed by researchers to improve the stability of perovskite light-emitting diodes (PeLEDs), which can be divided into two categories: (1) passivation of defects and (2) inhibition of ion migration.¹⁵ The addition of defect passivation additives to the perovskite layer inhibits the increase of non-radiative recombination centers and improves the operational stability of PeLEDs. Lin *et al.*¹⁶ spin-coated DDS solution on the surface of perovskite films and annealed the perovskite films with DDS modified layer, which effectively passivated the surface defects and reduced the non-radiative recombination centers, and further improved the stability as well as the luminescence efficiency. In addition, the construction of core/shell grain structure, in which 3D bulk grains are covered by a shell layer such as bulk organic cations, may be a better strategy to achieve long lifetime PeLEDs.¹⁵ The grain boundaries in all directions are passivated by the large grain shells, thus inhibiting ion migration, and CsPbBr_3 – Cs_4PbBr_6 microcrystals were prepared for the first time by Hu *et al.*,¹⁷ the embedded composite structure has excellent

Key Laboratory of Luminescence and Optical Information, Ministry of Education, Institute of Optoelectronic Technology, Beijing Jiaotong University, Beijing, 100044, China. E-mail: lxyi@bjtu.edu.cn

† Electronic supplementary information (ESI) available. See DOI: <https://doi.org/10.1039/d3ra03947a>



luminescent properties and good stability. The photoluminescence (PL) intensity decays by only 20% when placed in ambient for 2 months. As for the low exciton binding energy of perovskite, low quantum efficiency of perovskite thin films, strategies such as monitoring the growth, morphology, and grain size of perovskite can result in a higher PLQY.¹⁸ Alternatively, a new quantum-constrained structure can be constructed, for example, by converting continuous $[\text{PbX}_6]^{4-}$ octahedra into isolated octahedra in perovskites.¹⁹ Akkerman *et al.*²⁰ introduced the Cs_4PbBr_6 phase and embedded nanocrystals of CsPbBr_3 in the photoactive Cs_4PbBr_6 forming a $\text{Cs}_4\text{PbBr}_6/\text{CsPbBr}_3$ core–shell structure, electrons and holes formed in CsPbBr_3 are spatially confined by Cs_4PbBr_6 , which can significantly improve the luminescence efficiency.²¹

The 0-D Cs_4PbBr_6 phase of CsPbBr_3 , known for its lattice matching provides ideal passivation and efficient exciton confinement, has served as an inspiration for our research. This has led us to introduce the Cs_4PbBr_6 phase to prepare $\text{CsPbBr}_3\text{–Cs}_4\text{PbBr}_6$ composite films. As a derivative of CsPbBr_3 , Cs_4PbBr_6 has a zero-dimensional crystal structure with a wide band gap (~ 3.9 eV),²² where the $[\text{PbBr}_6]^{4-}$ octahedron is completely separated by Cs^+ ions, confining the charge carriers to two dimensions.²³ Owing to the Cs_4PbBr_6 lattice matches well with CsPbBr_3 , Cs_4PbBr_6 can effectively passivate the vacancy defects in CsPbBr_3 and reduces the number of defects.²⁴ Consequently, the $\text{CsPbBr}_3\text{–Cs}_4\text{PbBr}_6$ films exhibit enhanced stability against moisture and oxygen, which represents a marked improvement over the 3D CsPbBr_3 films of inferior crystalline quality. The wide band gap of Cs_4PbBr_6 ($E_g \approx 3.9$ eV), CsPbBr_3 is embedded in Cs_4PbBr_6 , which inhibits ion migration and improves the radiative recombination.²⁵ Coupled with the high absorption in the ultraviolet (UV) region, superior stability, and high PLQY, these properties endow $\text{CsPbBr}_3\text{–Cs}_4\text{PbBr}_6$ composite films with excellent performance capabilities in LEDs applications.

The fabrication of high-quality inorganic perovskite films through a specialized method is crucial for enhancing the optoelectronic device performance. Researchers usually use solution method to prepare perovskite films. Because of the poor solubility of CsX in the precursor solution, it would be an obstacle for the reproducibility of smooth surface and full coverage films.²⁶ In contrast, the vacuum evaporation method allows for effortless deposition of multi-layer films, characterized by superior flatness and morphology. Despite its potential, this method remains relatively underreported in the literature.²⁷

In this paper, a dual-source vacuum co-evaporation method is proposed for the fabrication of $\text{CsPbBr}_3\text{–Cs}_4\text{PbBr}_6$ films. By adjusting the evaporation rate ratio in co-evaporation, we can flexibly adjust the molar ratio of the components. As the $\text{CsBr}/\text{PbBr}_2$ molar ratio increased from 1 to 1.58, a blue shift in the photoluminescence (PL) wavelength from 520 to 508 nm was observed. The thin film prepared is compact, free of pinholes, and exhibits optimal coverage and high repeatability. To further improve the crystallization characteristics of the film, the effects of annealing temperature and annealing time in rapid air annealing on $\text{CsPbBr}_3\text{–Cs}_4\text{PbBr}_6$ films were studied in detail. Under optimal annealing conditions, the $\text{CsPbBr}_3\text{–Cs}_4\text{PbBr}_6$ is able to achieve excellent PL performance and stability. The

annealed film exhibited dense, even after being placed under ambient air (average humidity 48%) for 100 days, it was able to retain 85% of its photoluminescence (PL) intensity. Utilizing this annealed composite film, an $\text{Ag}/\text{N-Si}/\text{CsPbBr}_3\text{–Cs}_4\text{PbBr}_6/\text{NiO}/\text{ITO}$ structured LED was constructed. The maximum brightness can reach 957 cd m^{-2} , and unencapsulated device operate continuously for 12 hours under direct current drive with merely a 10% attenuation, even under ambient air conditions.

2. Experimental

The substrates were meticulously cleaned using deionized water, detergent, acetone, and absolute ethanol, followed by drying with flowing nitrogen gas. Deposition materials, namely CsBr (99.9%) and PbBr_2 (99.9%) powders, were prepared after undergoing water removal treatment, and were then placed in two thermal evaporation crucibles.²⁸ The evaporation chamber was subjected to a vacuum level of 3×10^{-3} pa, with the thickness of the films and the evaporation rate of CsBr and PbBr_2 monitored using a quartz crystal monitor. To enhance the crystalline quality of the films, they were annealed in ambient air (RTP-500) between temperatures of 200 °C and 350 °C. The PeLEDs have a device structure of Ag (50 nm)/N-type Si/ $\text{CsPbBr}_3\text{–Cs}_4\text{PbBr}_6$ (180 nm)/ NiO (40 nm)/ITO (200 nm). The LED emitting area was 0.2 cm^2 . Initially, $\text{CsPbBr}_3\text{–Cs}_4\text{PbBr}_6$ films were deposited on N-type Si (100) substrates through thermal co-evaporation (SD400M). Following this, NiO films were deposited on the $\text{CsPbBr}_3\text{–Cs}_4\text{PbBr}_6$ films as a hole transport layer *via* magnetron sputtering technique (XSYZKFF-1200), utilizing a sputtering power of 100 W and gas flow rates of 45 and 10 sccm for Ar and O_2 , respectively. The sputtering pressure is 0.55 pa, with a sputtering rate of 0.05 \AA s^{-1} . The ITO electrode was deposited on the film's surface with a radio frequency (RF) power of 60 W, Ar flow rate of 40 sccm, the sputtering pressure is 0.55 pa, and sputtering rate of 0.6 \AA s^{-1} . The Ag electrode was placed on the backside of the N-type Si substrate with a sputtering power of 150 W, Ar flow rate of 40 sccm, the sputtering pressure is 0.58 pa, and sputtering rate of 9 \AA s^{-1} .

Absorption spectra of the $\text{CsPbBr}_3\text{–Cs}_4\text{PbBr}_6$ films were recorded using an UV-VIS-NIR scanning spectrophotometer (UV-3101PC). The photoluminescence (PL) spectra were measured by a 325 nm He–Cd laser and a fluorescence spectrophotometer (FLS920) as the light source and detector.²⁹ Each device was carefully calibrated before every measurement to ensure maximum accuracy and reliability. The crystallinity and phases of films were inspected *via* the X-ray diffraction (XRD, Bruker D8 Advance, with $\text{Cu K}\alpha$ radiation ($\lambda = 1.54 \text{ \AA}$)) pattern. The surface morphologies of thin films were observed by scanning electron microscope (SEM, Oxford, JSM-7800F(Prime), accelerating voltage of 15 kV, resolution is 0.8 nm, spot size of 50 nm, Working distance is 10 mm). The element ratios of the films were measured by energy dispersive spectroscopy (EDS, X-MaxN50 Aztec). Time-resolved photoluminescence (TRPL) spectra were measured by steady-state and time-resolved photoluminescence spectrometer (FLS1000). Transmitted electron

microscopy (TEM) images were acquired by the JEOL 1400 transmission electron microscope with an acceleration voltage of 80 keV, spot size of 2 nm, to which an Oxford energy dispersive X-ray spectroscopy (EDS) system X-max50 was coupled for EDS-TEM mapping analysis. High resolution TEM (HRTEM) images were acquired by the JEOL 1400F high resolution transmission electron microscope (acceleration voltage of 200 kV, minimum spot size of 0.2 nm, resolution of 0.19 nm). The EL performances including current density, luminance, and operational stability (without encapsulation) of the perovskite LEDs were recorded simultaneously by a commercial measurements system (a programmable Keithley 2400 source meter and a Photo Research Spectra Scan PR655).

3. Results and discussion

3.1. Optical spectra and crystal structures of as-deposited $\text{CsPbBr}_3\text{-Cs}_4\text{PbBr}_6$ films

By regulating the ratio of $\text{CsBr}/\text{PbBr}_2$ precursors, we anticipate that the CsPbBr_3 films, when enveloped by excess CsBr or PbBr_2 vapor, could be transformed into the derivative phase Cs_4PbBr_6 or CsPb_2Br_5 . Previous literature has reported that the presence of a derivative phase can not only improve light capture in the UV region,³⁰ but also due to lattice matching, it can passivate interfacial defects.³¹ Moreover, the absence of a mesophase obviates the need for introducing foreign organic additives, thereby improving stability. While the Cs_2PbBr_5 phase has inactive photoluminescence³² and a large indirect band gap of about 3.1 eV, detrimental to device performance, the stronger Coulomb interaction due to the spatial confinement of CsPbBr_3 grains within the Cs_4PbBr_6 host lattice could enhance the carrier radiative recombination process.³³

In this study, a composite film of $\text{CsPbBr}_3\text{-Cs}_4\text{PbBr}_6$ was fabricated through thermal evaporation. Given the low charge transport of Cs_4PbBr_6 , the relative content of CsPbBr_3 and Cs_4PbBr_6 required careful regulation for effective charge injection.³⁴ This was achieved by adjusting the evaporation rate ratio

of the precursors (CsBr and PbBr_2), resulting in a series of Cs-Pb-Br films with varied $\text{CsBr}/\text{PbBr}_2$ molar ratios. The $\text{CsBr}/\text{PbBr}_2$ ratio is approximately estimated by an energy-dispersive spectrometer (EDS) measurement (ESI Table S1†). Through examination of the XRD patterns of films with different ratios (as shown in Fig. 1), it was noted that the transformation of the films from the cubic CsPbBr_3 phase to the coexistence of CsPbBr_3 and Cs_4PbBr_6 phases as the Cs/Pb ratio transitions from 1/1 to 1.58/1. The cubic structure of CsPbBr_3 produces diffraction peak at approximately 15.8° , 22.4° , 31.9° , and 35.7° corresponding to the (100), (110), (200) and (210) crystal planes (PDF #75-0412), respectively. As the $\text{CsBr}/\text{PbBr}_2$ ratio increases, the products show diffraction peaks at about 12.9° , 20.1° , 21.8° , 25.4° , 28.6° and 30.3° , corresponding to the (110), (113), (104), (024), (214) and (223) crystal planes of the rhombic phase (PDF #73-2478) of Cs_4PbBr_6 . It is clear that a higher Cs/Pb ratio results in a higher content of Cs_4PbBr_6 . $\text{Cs}/\text{Pb} = 1.34$ exhibits stronger diffraction peaks on the (104) and (223) crystal planes, suggesting superior crystalline quality at this ratio. Additionally, it was observed that as the Cs/Pb ratio increases, the full width at half peak (FWHM) of the diffraction peak on the (100) crystal plane of CsPbBr_3 becomes wider. According to the Debye-Scherrer formula ($D = K\lambda/B \cos \theta$, where B is the FWHM and D is the mean diameter of the crystal domains),³⁵ this indicates a decrease in the size of CsPbBr_3 grains.

Further examination was conducted on the optical properties of the four films at different ratios. The PL spectra Fig. 2 illustrate that as the Cs/Pb ratio ranged from 1 : 1 to 1.58 : 1, the luminescence peak shifted from 520 nm to 508 nm. Concurrently, the film luminescence changed from green to cyan. We speculate that when the composites incorporate a larger proportion of CsBr , according to the XRD patterns, a high $\text{CsBr}/\text{PbBr}_2$ ratio generally yields high content of Cs_4PbBr_6 , the Cs -rich Cs_4PbBr_6 phase possesses a 0D structure with $[\text{PbBr}_6]^{4-}$ octahedra completely isolated by Cs^+ cations, which can serve as a barrier to break the connectivity of $[\text{PbBr}_6]^{4-}$ in CsPbBr_3 and impede the growth of CsPbBr_3 , the spatial confinement effect is enhanced resulting in the decrease of CsPbBr_3 grain size,

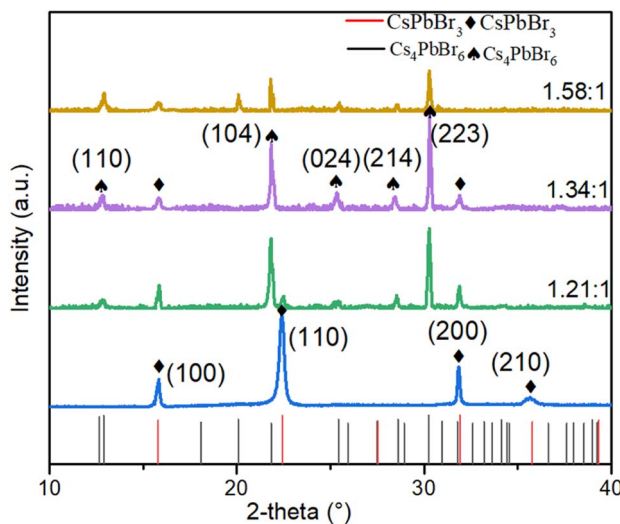


Fig. 1 XRD patterns of as-deposited films with different molar ratios.

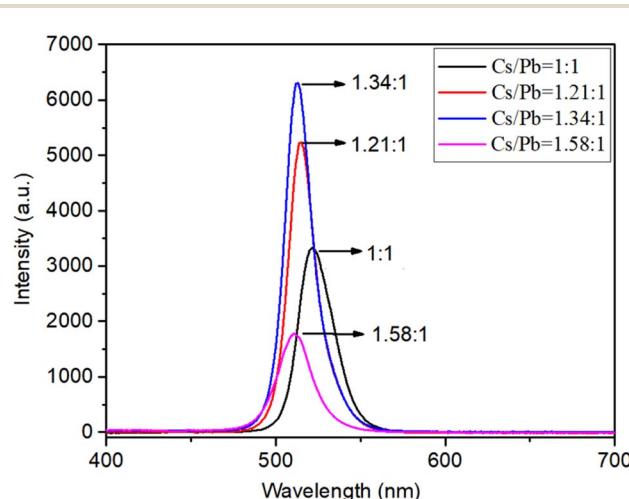


Fig. 2 PL spectra of Cs-Pb-Br films with different molar ratios.



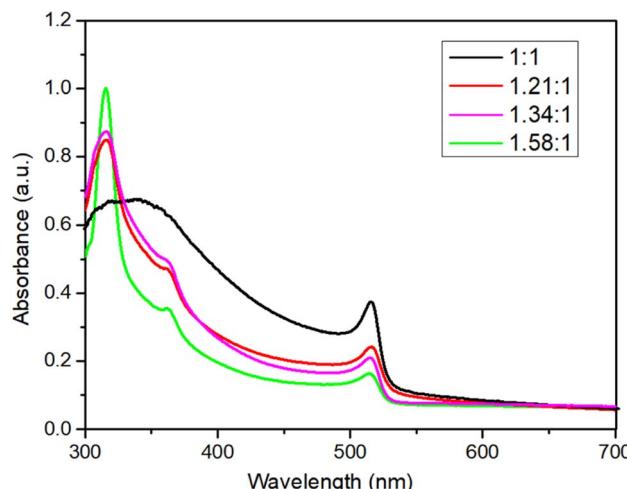


Fig. 3 The absorption spectra of Cs–Pb–Br films with different molar ratios.

causing a blue shift in the PL peak position.¹⁸ This suggests that the electrons and holes formed in CsPbBr_3 are spatially constrained by Cs_4PbBr_6 , resulting in enhanced PL.³⁶ The strongest PL intensity was observed at a Cs/Pb ratio of 1.34, time-resolved photoluminescence (TRPL) spectra are shown in Fig. S1,[†] suggesting superior optoelectronic quality and high radiative recombination rate in these films. The ultraviolet-visible absorption spectra in Fig. 3 exhibited two absorption peaks at 317 nm and 514 nm, ascribed to Cs_4PbBr_6 and CsPbBr_3 , respectively. A progressive increase in the intensity of the absorption band at 317 nm was observed as the Cs/Pb ratio rose from 1.21 to 1.58, which implies an increase in the Cs_4PbBr_6 phase content within the nanocomposite corresponding to the increased CsBr content in the precursor.

Surface morphologies of the CsPbBr_3 and CsPbBr_3 – Cs_4PbBr_6 composite films were further investigated using SEM. As shown in Fig. 4, the films appear dense and devoid of pinholes, featuring two distinct grain morphologies as the Cs/Pb ratio increases. A transmission electron microscopy (TEM) image

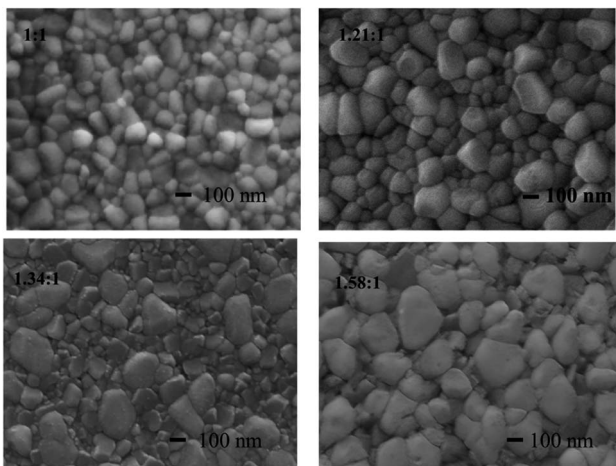


Fig. 4 SEM images of as-deposited films with different molar ratios.

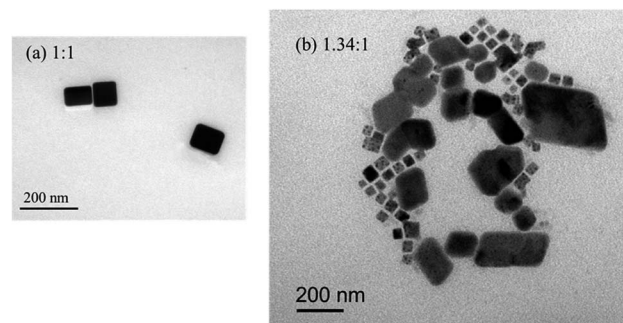


Fig. 5 TEM images of (a) 1 : 1 thin film (b) 1.34 : 1 thin film.

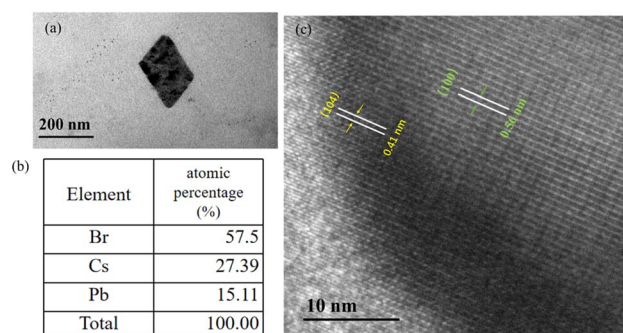


Fig. 6 (a) TEM images of (b) element atomic percentage of (c) HR-TEM images of CsPbBr_3 – Cs_4PbBr_6 core–shell structure.

(Fig. 5(a)) of a specimen made by scraping a Cs/Pb = 1 : 1 thin film exhibited the similar cubic CsPbBr_3 structure, and on further increasing the molar ratio to Cs/Pb = 1.34/1 reveals that two crystal morphologies appear in the image (Fig. 5(b)). The larger rhombic shaped crystal with smooth outer surface and almost sharp edges (crystal size of about 187 nm) and the cubic shaped CsPbBr_3 small grains with an average size of 54 nm, which is similar to the previously reported TEM results for the CsPbBr_3 – Cs_4PbBr_6 material.³⁷ Therefore, a high-resolution TEM (HR-TEM) image was acquired to identify the rhombic shaped phase. Fig. 6(c) shows a HR-TEM image exhibiting different sets of lattice fringes, which can be attributed to the CsPbBr_3 and Cs_4PbBr_6 phases. Fig. 6(c) exhibited a lattice spacing of 0.56 nm in inner layer, which is consistent with the (100) crystal plane, confirming the cubic CsPbBr_3 structure. As for grain edges, a lattice spacing of 0.41 nm, corresponding to the (104) crystal plane, confirming the rhombohedral Cs_4PbBr_6 structure. Therefore, the HR-TEM results demonstrate that CsPbBr_3 are embedding into the rhombohedral prism of the Cs_4PbBr_6 structure, forming core–shell CsPbBr_3 – Cs_4PbBr_6 structure. The energy-dispersive spectroscopy (EDS) in Fig. 6(b) confirm the conclusion. Due to the existence of the thin shell layer, size of the CsPbBr_3 would reduce resulting in a blue shift,³⁸ this is consistent with PL spectra and SEM images.

Based on the results obtained from PL spectra and XRD patterns, it is evident that the films exhibit high photoluminescence intensity and good crystalline quality when the Cs/Pb ratio is 1.34. With the increasing Cs/Pb ratio, the film



luminescence changes from green to cyan due to the shift of the luminescence peak position, which deviates from our desired luminescence color. In addition, too much CsBr leads to the water instability of $\text{CsPbBr}_3\text{-Cs}_4\text{PbBr}_6$ film. Therefore, for further study and the fabrication of electroluminescent devices, we focus on the film with a CsBr/PbBr₂ ratio of 1.34.

3.2. Effect of air-annealing temperature on the $\text{CsPbBr}_3\text{-Cs}_4\text{PbBr}_6$ films

In order to further improve the crystalline quality of the films and reduce the defect concentration, we employed rapid thermal annealing on $\text{CsPbBr}_3\text{-Cs}_4\text{PbBr}_6$ films (with a Cs/Pb ratio of 1.34) in an ambient air atmosphere. This allowed us to observe the effect of various annealing temperatures (ranging from 200 °C to 350 °C) on the luminescence properties and crystallinity of the films.

Fig. 7(a) illustrates the photoluminescence (PL) spectra of the annealed composite films at different temperatures. For the annealed samples, it is observed that as the annealing temperature increases, the PL intensity strengthens constantly. The strongest PL intensity is observed in the $\text{CsPbBr}_3\text{-Cs}_4\text{PbBr}_6$ film annealed at 300 °C, indicating that the film has the best photoluminescence with lower defects. After that, the PL intensity decreases as the annealing temperature continues to increase. In addition, the PL emission peaks of the annealed samples exhibit a red shift as the annealing temperature increases, in comparison to the unannealed films. This may be attributed to the increase in grain size.

Fig. 7(b) exhibits the time-resolved photoluminescence (TRPL) spectra of the films at different annealing temperatures and a double exponential fit to the PL lifetime. The deduced decay lifetimes are shown in Table S2.† Typically, the slow decay (τ_2) component represents the process of trap-assisted radiative recombination within the bulk perovskite phase, while the fast decay (τ_1) component reflects the carrier quenching at the interface.³⁹ The recombination lifetimes of both the surface and bulk phase of the annealed films were substantially prolonged, from 1.41 ns and 6.34 ns to 2.02 ns and 26.24 ns, respectively. When compared to the unannealed films, this signifies

a significant reduction in both the surface defect density and bulk phase defect density of the films.⁴⁰

The XRD patterns of the $\text{CsPbBr}_3\text{-Cs}_4\text{PbBr}_6$ films at different annealing temperatures are depicted in Fig. 8. We noted the disappearance of the (104) crystal plane of Cs_4PbBr_6 and the appearance of the (111) crystal plane, correlating to the CsBr phase (PDF#78-0615), with the increase in annealing temperature. Also with the increase of annealing temperature, the diffraction intensity of the (100) crystal plane corresponding to CsPbBr_3 increases continuously below 300 °C, while the FWHM of the diffraction peak becomes narrower, and the grain size of CsPbBr_3 increases according to the Debye-Scherrer formula. This is likely a consequence of the gradual decomposition of Cs_4PbBr_6 into CsPbBr_3 and CsBr under the influence of ambient humidity, relevant to the reaction process $\text{Cs}_4\text{PbBr}_6 \rightarrow \text{CsPbBr}_3 + 3\text{CsBr}$. During this process, the decomposed CsPbBr_3 grains and the Cs_4PbBr_6 internal CsPbBr_3 grains continue to fuse and grow, and the crystallinity tends to be complete,^{41,42} eventually leading to enhanced fluorescence. This is also consistent with the conclusion obtained from PL spectra. The diffraction peak intensity of (100) and (223) crystal plane reaches the highest at

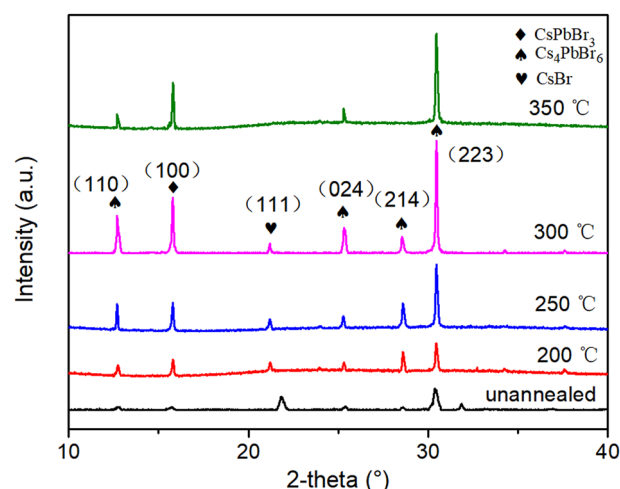


Fig. 8 XRD patterns of the films at different annealing temperatures.

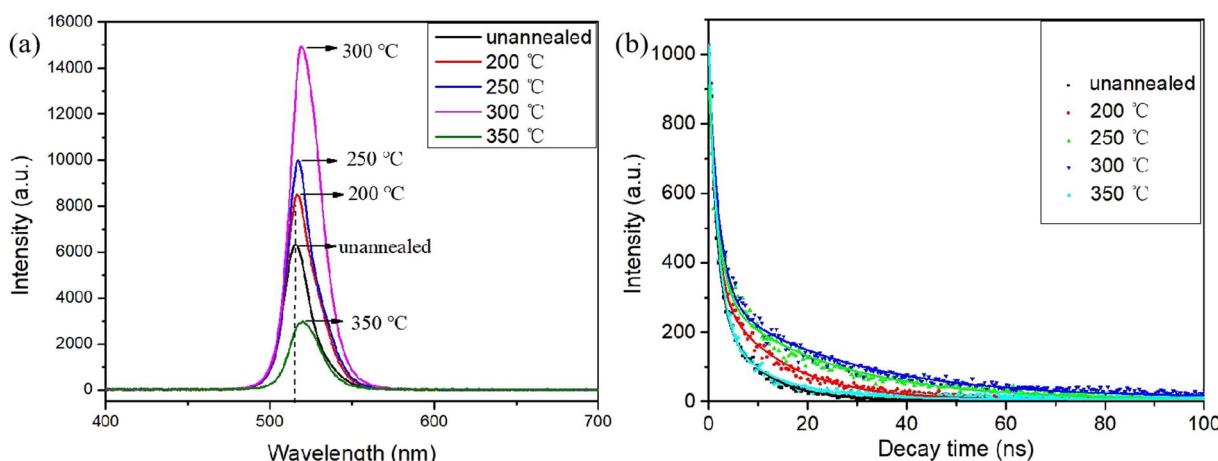


Fig. 7 (a) PL spectra (b) time-resolved photoluminescence (TRPL) spectra at different annealing temperatures.



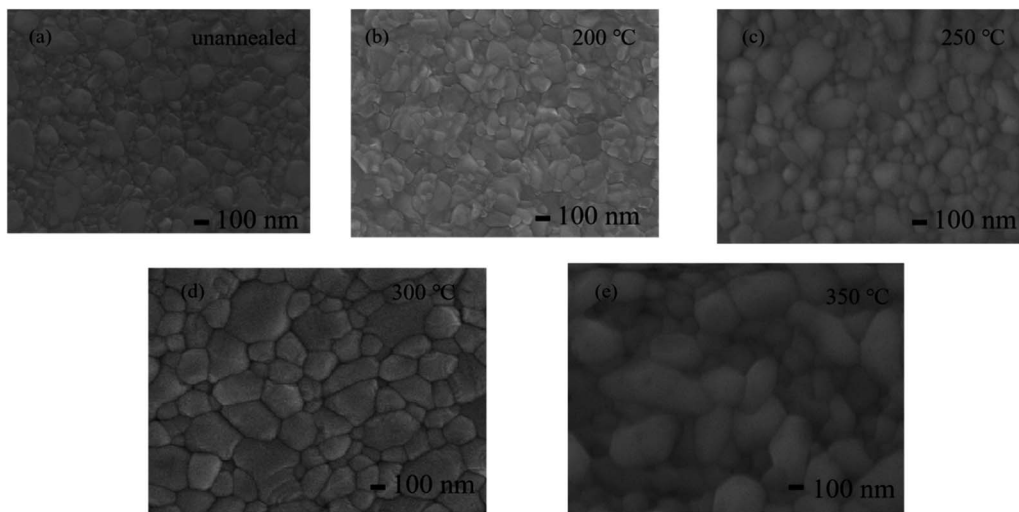


Fig. 9 SEM images of films annealed at different temperatures (a) unannealed (b) 200 °C (c) 250 °C (d) 300 °C (e) 350 °C.

300 °C. This implies a superior crystalline quality of the film at this temperature.

Fig. 9 presents the surface morphologies of the CsPbBr_3 - Cs_4PbBr_6 thin films annealed at varying temperatures and the grain size distribution statistics are shown in Fig. S2.† All the samples are uniform and dense, and the surface is fully covered. When the initial annealing temperature is low, the grain size increase is limited, and the grain boundaries become blurred. When the annealing temperature reaches 300 °C, the CsPbBr_3 grains located inside Cs_4PbBr_6 keep growing, the crystallinity tends to be complete,³⁴ the thin films become more dense, and the crystalline quality improves, which is beneficial to the device performance. This is consistent with the XRD observation. Therefore, we believe that CsPbBr_3 is embedded in the host Cs_4PbBr_6 and the annealing process is always accompanied by the growth and crystalline improvement of CsPbBr_3 .

3.3. Effect of air-annealing time on the CsPbBr_3 - Cs_4PbBr_6 films

We further investigated the impact of annealing conditions, including temperature and time, on CsPbBr_3 - Cs_4PbBr_6 .

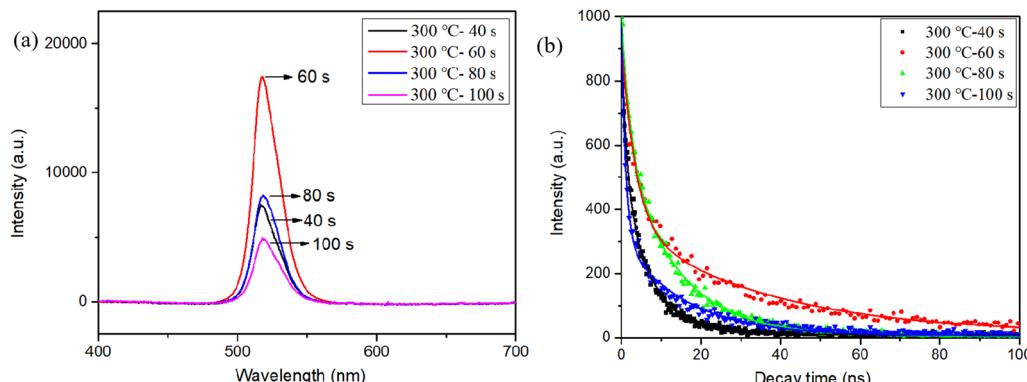


Fig. 10 (a) PL spectra (b) time-resolved photoluminescence (TRPL) spectra at different annealing times.

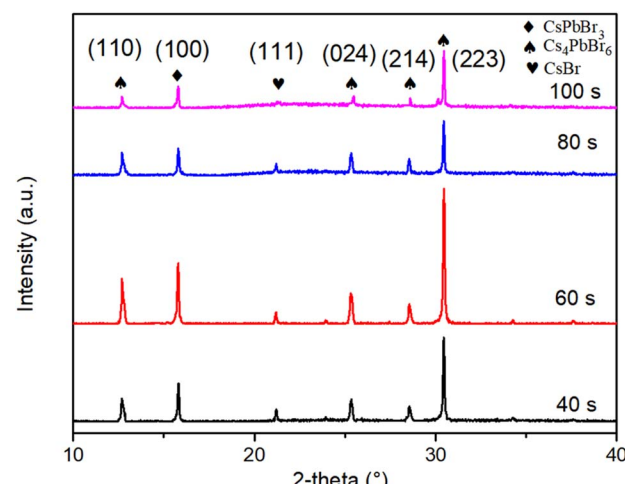


Fig. 11 XRD patterns of the films at different annealing times.

Fig. 10(a) shows the PL spectra of the films after annealing at 300 °C for 40–100 s in an ambient atmosphere. As the annealing time is extended, the PL intensity initially increases, peaking at



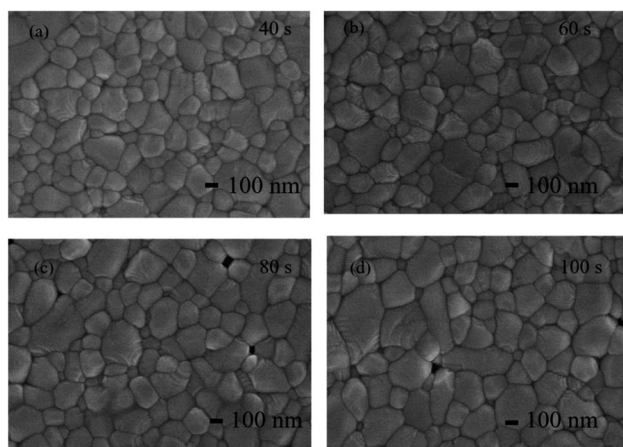


Fig. 12 SEM images of films annealed at 300 °C for different time (a) 40 s (b) 60 s (c) 80 s (d) 100 s.

60 s, before declining. This indicates that the proper annealing time is beneficial to the luminescence of the films. Meanwhile, the films at 60 s have longer surface and bulk phase combination lifetimes compared with other annealing times, as shown in Fig. 10(b). The deduced decay lifetimes are shown in Table S3,† τ_1 and τ_2 were significantly prolonged from 1.1 ns and 6.94 ns to 2.02 ns and 26.24 ns, respectively.

The XRD patterns of the films, presented in Fig. 11, reveal that as the annealing time increases, the intensity of the (100) and (223) crystal plane diffraction peak is the strongest at 60 s, indicating a good crystallinity at this time, and a proper annealing time is favorable for the luminescence and crystallinity.

SEM images of the films at different annealing times are presented in Fig. 12 and the domain size distribution histograms are shown in Fig. S3.† As the annealing time increases, the small grains corresponding to CsPbBr_3 grow together with Cs_4PbBr_6 grains and the grain size keeps increasing. However, with the further prolongation of annealing time, the film grains decompose and holes appear in the film leading to a decrease in crystallinity. The appropriate annealing time enhances the luminescence due to the improvement of crystal quality and the reduction of defects,²⁹ but the large grains produced by the excessively long annealing time lead to weakened carrier confinement and reduced luminescence intensity.¹³ Consequently, the optimal annealing condition for $\text{CsPbBr}_3\text{-Cs}_4\text{PbBr}_6$ films is determined to be 60 s at 300 °C. This condition yields the strongest PL intensity and the highest crystallinity.

3.4. Research on the stability of $\text{CsPbBr}_3\text{-Cs}_4\text{PbBr}_6$ thin films

The stability of the as-deposited and annealed $\text{CsPbBr}_3\text{-Cs}_4\text{PbBr}_6$ thin films were assessed by monitoring the attenuation of

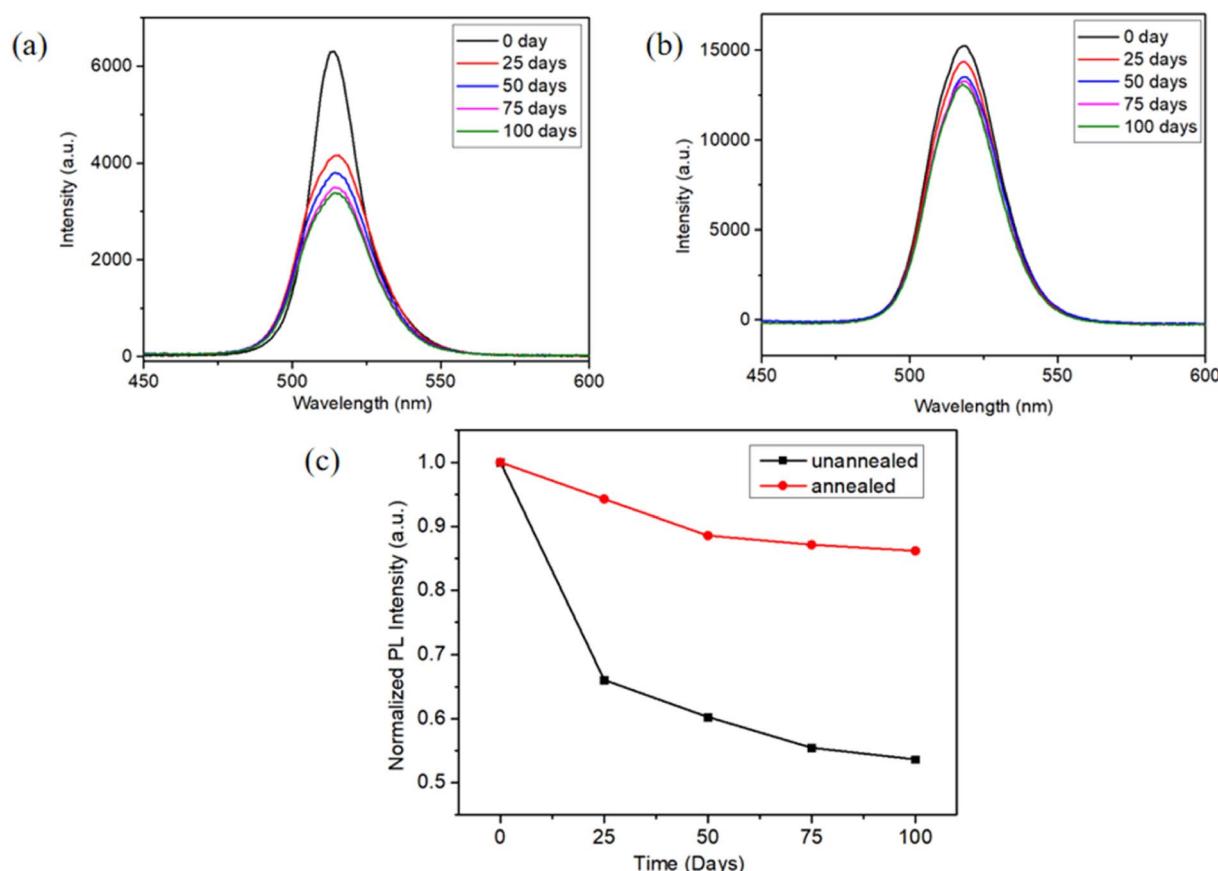


Fig. 13 (a) Peak positions of PL spectra of unannealed films, (b) peak positions of PL spectra of annealed films at different storage times in ambient air ($\lambda_{\text{ex}} = 325$ nm) (b) the PL intensity trend.



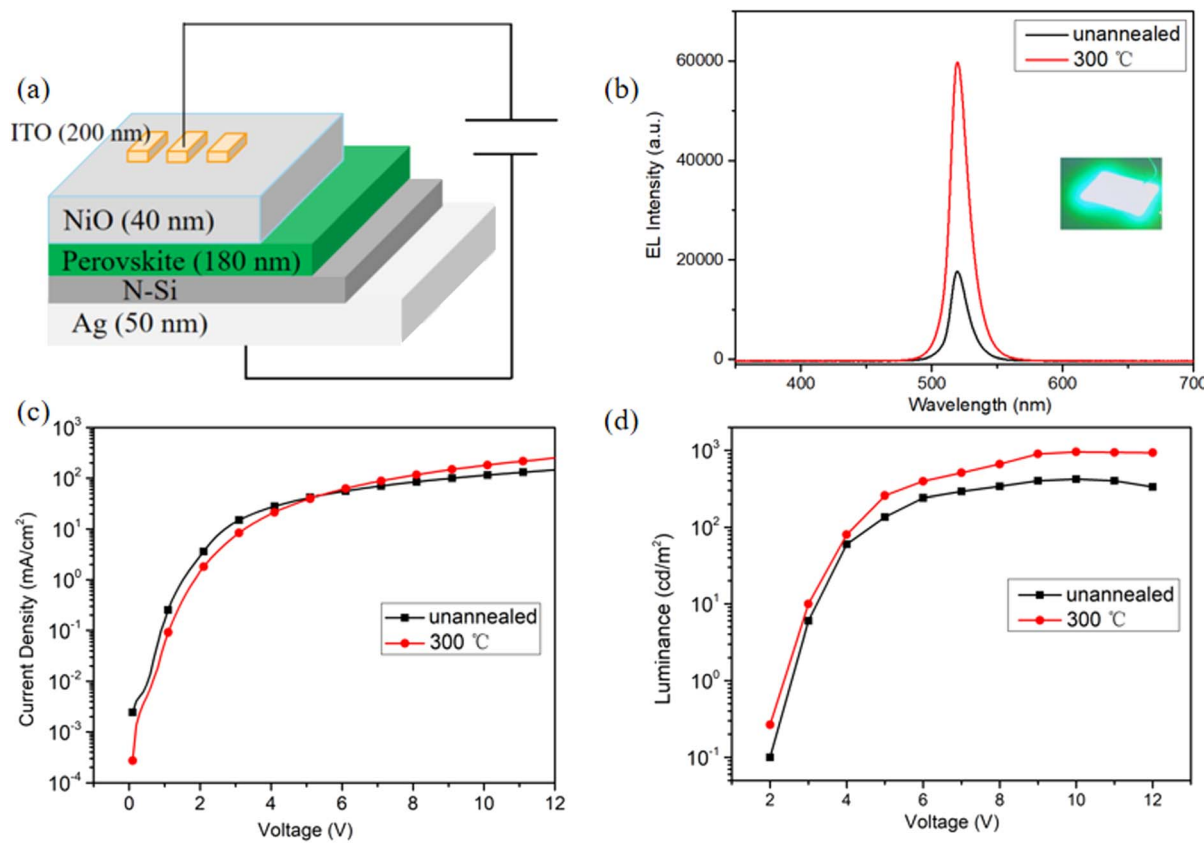


Fig. 14 (a) The devices architecture, (b) EL spectra, the insets show the photograph of the PeLEDs at an injection voltage of 10 V, (c) current density against voltage (J - V) curves of PeLEDs and (d) luminance against voltage (L - V) curves.

PL intensity in an ambient air environment at 48% relative humidity (RH), as depicted in Fig. 13(a) and (b). The images and surface morphology of the unannealed and annealed film after being placed in the air for 150 days are shown in Fig. S4 and S5.† Fig. 13(c) reveals that during the first 50 days of storage, a significant decay \sim 40% in PL intensity was observed in

unannealed film, however, the PL strength of the annealed film only attenuated by 12%. Over the following 50 days, the annealed film showed no significant decay in PL intensity. This could be due to annealing for improved crystallization quality and reduced defects. Meanwhile, sufficient passivation of the surface, which protected CsPbBr_3 from PL quenching.

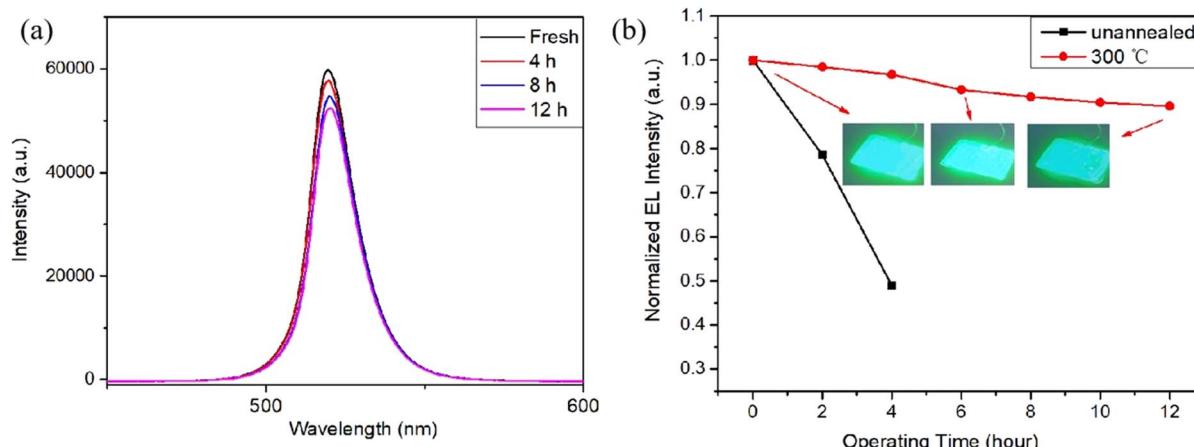


Fig. 15 (a) EL spectra acquired at different operating cycles under the same dc bias of 8 V and measurement conditions. (b) The EL intensity trend, the insets show the corresponding photographs of the PeLED after different running periods.

Environmental stability experiment showed the annealed film $\sim 15\%$ of the PL intensity loss after storage in ambient conditions for 100 days, signifying that the annealed films exhibit excellent environmental stability.

3.5. Study on the PeLEDs

Last, based on the best crystallinity and morphology, with the optimized parameters (Cs/Pb ratio of 1.34/1; perovskite film's thickness of 180 nm; annealing temperature of 300 °C with 60 s); we fabricated Perovskite light emitting diodes (PeLEDs) devices with the architecture of Ag/N-Si/CsPbBr₃-Cs₄PbBr₆/NiO/ITO. The devices architecture is shown in Fig. 14(a). The perovskite CsPbBr₃-Cs₄PbBr₆ layer serves as the emitting layer of carrier radiation recombination. The working mechanism of the device can be elucidated according to the fundamental physical processes of light-emitting diodes.^{43,44} Driven by forward voltage, green electroluminescence of the device is observed under dark conditions, the PeLEDs show good rectification characteristics, with small reverse current and the turn-on voltage of the device is ~ 3 V. Fig. 14(b) presents the electroluminescence (EL) spectrum of the devices, with an inset showing a photograph of our PeLEDs at an injection voltage of 10 V. The spectra shows an emission peak at 517 nm with the FWHM of 16 nm, indicating that our PeLEDs possess excellent color purity. Furthermore, devices with annealed CsPbBr₃-Cs₄PbBr₆ films exhibit higher EL intensity compared to the unannealed films, which indicates that the enhancement of films quality and device performance by rapid annealing in ambient air. After annealing, the devices performed best with a maximum luminance (L_{max}) of 957 cd m⁻². Importantly, our unencapsulated PeLEDs operate continuously for 12 hours under direct current drive with only a 10% attenuation in ambient air conditions, demonstrating their relatively superior stability in Fig. 15. Compared to reference devices using traditional organic carrier injection layers such as PEDOT:PSS,⁴⁵ our device provides significantly improved operational stability.

4. Conclusion

In conclusion, high quality CsPbBr₃-Cs₄PbBr₆ films were successfully prepared *via* a co-evaporation method, guided by the careful adjustment of the CsBr/PbBr₂ molar ratio. The enhancement in the optical properties and stability of the films was observed with an increase in Cs/Pb ratio, with the optimal ratio found to be 1.34/1. A luminescence peak near 515 nm was identified in the films with a narrow FWHM. An air rapid annealing treatment was utilized to further improve the films' crystalline quality. The optimal PL intensity and crystalline quality were achieved at an annealing temperature of 300 °C for 60 s. These annealed films exhibited excellent stability, maintaining 85% of their PL intensity after 100 days in ambient air conditions. Based on these films, we constructed all-inorganic structured PeLEDs (Ag (50 nm)/N-Si/CsPbBr₃-Cs₄PbBr₆ (180 nm)/NiO (40 nm)/ITO (200 nm)), the unencapsulated device showed only a 10% decay after 12 h, under ambient air

condition. This work presents a promising approach for future design and development of stable perovskite-based LEDs.

Data availability

All data generated or analysed during this study are included in this published article.

Conflicts of interest

The authors declare that they have no competing interests.

Author contributions

Tianxinyu Bai wrote the main manuscript. Shenwei Wang, Kexin Zhang and Chunyang Chu, Yingqiang Sun read and approved the final manuscript. Lixin Yi: funding acquisition.

Acknowledgements

This study was supported in part by grants from the National Natural Science Foundation of China (Grant No. 61975008). It was also supported by the Key Laboratory of Luminescence and Optical Information of China in Beijing Jiaotong University.

References

- 1 C. Tian, K. Lin, J. Lu, W. Feng, P. Song, L. Xie and Z. Wei, *Small Methods*, 2020, **4**, 1900476.
- 2 Y. Kim, H. Cho, J. H. Heo, T. Kim, N. Myoung, C. Lee, S. H. Im and T. Lee, *Adv. Mater.*, 2015, **27**, 1248–1254.
- 3 Z. Xiao, R. A. Kerner, L. Zhao, N. L. Tran, K. M. Lee, T. Koh, G. D. Scholes and B. P. Rand, *Nat. Photonics*, 2017, **11**, 108–115.
- 4 J. Xue, R. Wang, X. Chen, C. Yao, X. Jin, K. Wang, W. Huang, T. Huang, Y. Zhao, Y. Zhai, D. Meng, S. Tan, R. Liu, Z. Wang, C. Zhu, K. Zhu, M. C. Beard, Y. Yan and Y. Yang, *Science*, 2021, **371**, 636–640.
- 5 Q. Gao, J. Qi, K. Chen, M. Xia, Y. Hu, A. Mei and H. Han, *Adv. Mater.*, 2022, **34**, 2200720.
- 6 J. S. Kim, J. Heo, G. Park, S. Woo, C. Cho, H. J. Yun, D. Kim, J. Park, S. Lee, S. Park, E. Yoon, N. C. Greenham and T. Lee, *Nature*, 2022, **611**, 688–694.
- 7 K. Jia, L. Song, Y. Hu, X. Guo, X. Liu, C. Geng, S. Xu, R. Fan, L. Huang, N. Luan and W. Bi, *ACS Appl. Mater. Interfaces*, 2020, **12**, 15928–15933.
- 8 W. Li, Y. Xu, D. Wang, F. Chen and Z. Chen, *Org. Electron.*, 2018, **57**, 60–67.
- 9 J. Lei, F. Gao, H. Wang, J. Li, J. Jiang, X. Wu, R. Gao, Z. Yang and S. F. Liu, *Sol. Energy Mater. Sol. Cells*, 2018, **187**, 1–8.
- 10 D. Zhao, W. Ke, C. R. Grice, A. J. Cimaroli, X. Tan, M. Yang, R. W. Collins, H. Zhang, K. Zhu and Y. Yan, *Nano Energy*, 2016, **19**, 88–97.
- 11 J. Liang, C. Wang, Y. Wang, Z. Xu, Z. Lu, Y. Ma, H. Zhu, Y. Hu, C. Xiao, X. Yi, G. Zhu, H. Lv, L. Ma, T. Chen, Z. Tie, Z. Jin and J. Liu, *J. Am. Chem. Soc.*, 2016, **138**, 15829–15832.



12 X. Hu, X. Zhang, L. Liang, J. Bao, S. Li, W. Yang and Y. Xie, *Adv. Funct. Mater.*, 2014, **24**, 7373–7380.

13 Y. Fu, Q. Zhang, D. Zhang, Y. Tang, L. Shu, Y. Zhu and Z. Fan, *Adv. Funct. Mater.*, 2020, **30**, 2002913.

14 L. Chu, W. Ahmad, W. Liu, J. Yang, R. Zhang, Y. Sun, J. Yang and X. A. Li, *Nano-Micro Lett.*, 2019, **11**, 16.

15 S. Woo, J. S. Kim and T. Lee, *Nat. Photonics*, 2021, **15**, 630–634.

16 J. Lin and T. Wang, *Sol. Energy Mater. Sol. Cells*, 2022, **3**, 3–4.

17 G. Hu, W. Qin, M. Liu, X. Ren, X. Wu, L. Yang and S. Yin, *J. Mater. Chem. C*, 2019, **7**, 4733–4739.

18 P. Du, L. Wang, J. Li, J. Luo, Y. Ma, J. Tang and T. Zhai, *Adv. Opt. Mater.*, 2022, **10**, 2101770.

19 P. Du, J. Li, L. Wang, L. Sun, X. Wang, X. Xu, L. Yang, J. Pang, W. Liang, J. Luo, Y. Ma and J. Tang, *Nat. Commun.*, 2021, **12**, 4751.

20 Q. A. Akkerman, S. Park, E. Radicchi, F. Nunzi, E. Mosconi, F. De Angelis, R. Brescia, P. Rastogi, M. Prato and L. Manna, *Nano Lett.*, 2017, **17**, 1924–1930.

21 X. Xiong, H. Liu, W. Wang, J. Gong, X. Chen, Y. Zhao, T. Tian and L. Wang, *Luminescence*, 2021, **36**, 631–641.

22 L. Wang, H. Liu, Y. Zhang and O. F. Mohammed, *ACS Energy Lett.*, 2020, **5**, 87–99.

23 Z. Ma, Z. Liu, S. Lu, L. Wang, X. Feng, D. Yang, K. Wang, G. Xiao, L. Zhang, S. A. T. Redfern and B. Zou, *Nat. Commun.*, 2018, **9**, 4506.

24 Z. Wang, Y. Zhang, X. Liu, Y. Yu, F. Xu, J. Ding, X. Liang, K. Yang and W. Xiang, *Adv. Mater. Technol.*, 2021, **6**, 2100654.

25 X. Lian, X. Wang, Y. Ling, E. Lochner, L. Tan, Y. Zhou, B. Ma, K. Hanson and H. Gao, *Adv. Funct. Mater.*, 2019, **29**, 1807345.

26 J. Li, P. Du, S. Li, J. Liu, M. Zhu, Z. Tan, M. Hu, J. Luo, D. Guo, L. Ma, Z. Nie, Y. Ma, L. Gao, G. Niu and J. Tang, *Adv. Funct. Mater.*, 2019, **29**, 1903607.

27 Y. Hu, Q. Wang, Y. Shi, M. Li, L. Zhang, Z. Wang and L. Liao, *J. Mater. Chem. C*, 2017, **5**, 8144–8149.

28 T. Bai, S. Wang, L. Bai, K. Zhang, C. Chu and L. Yi, *Nanoscale Res. Lett.*, 2022, **17**, 69.

29 L. Y. Bai, S. W. Wang, Y. W. Zhang, K. X. Zhang and L. X. Yi, *J. Lumin.*, 2020, **227**, 117592.

30 H. Li, G. Tong, T. Chen, H. Zhu, G. Li, Y. Chang, L. Wang and Y. Jiang, *J. Mater. Chem. A*, 2018, **6**, 14255–14261.

31 J. Cao, X. Zeng, W. Li, L. Lv, C. Yan, H. Huang, J. Lu and W. Yang, *Appl. Mater. Today*, 2023, **30**, 101733.

32 T. Chen, C. Wang and J. Bao, *2021 IEEE 16th Nanotechnology Materials and Devices Conference (NMDC)*, 2021, pp.1–5.

33 X. Lian, X. Wang, Y. Ling, E. Lochner, L. Tan, Y. Zhou, B. Ma, K. Hanson and H. Gao, *Adv. Funct. Mater.*, 2019, **29**, 1807345.

34 K. Lin, C. Yan, R. P. Sabatini, W. Feng, J. Lu, K. Liu, D. Ma, Y. Shen, Y. Zhao, M. Li, C. Tian, L. Xie, E. H. Sargent and Z. Wei, *Adv. Funct. Mater.*, 2022, **32**, 2200350.

35 H. Cho, S. Jeong, M. Park, Y. Kim, C. Wolf, C. Lee, J. H. Heo, A. Sadhanala, N. Myoung, S. Yoo, S. H. Im, R. H. Friend and T. Lee, *Science*, 2015, **350**, 1222–1225.

36 M. Jo, N. Yasuhara, K. Ishida, K. Kawamoto and S. Fukatsu, *Phys. E*, 2004, **21**, 354–357.

37 V. Naresh, T. Jang, Y. Pang and N. Lee, *Nanoscale*, 2022, **14**, 17789–17801.

38 J. Xu, W. Huang, P. Li, D. R. Onken, C. Dun, Y. Guo, K. B. Ucer, C. Lu, H. Wang, S. M. Geyer, R. T. Williams and D. L. Carroll, *Adv. Mater.*, 2017, **29**, 1703703.

39 D. Shi, V. Adinolfi, R. Comin, M. Yuan, E. Alarousu, A. Buin, Y. Chen, S. Hoogland, A. Rothenberger, K. Katsiev, Y. Losovoj, X. Zhang, P. A. Dowben, O. F. Mohammed, E. H. Sargent and O. M. Bakr, *Science*, 2015, **347**, 519–522.

40 L. Liu, S. Yang, P. Liu and Y. Chen, *Sol. Energy*, 2022, **232**, 320–327.

41 Y. Ling, L. Tan, X. Wang, Y. Zhou, Y. Xin, B. Ma, K. Hanson and H. Gao, *J. Phys. Chem. Lett.*, 2017, **8**, 3266–3271.

42 X. Xiong, H. Liu, W. Wang, J. Gong, X. Chen, Y. Zhao, T. Tian and L. Wang, *Luminescence*, 2021, **36**, 631–641.

43 S. Zhuang, X. Ma, D. Hu, X. Dong and B. Zhang, *Ceram. Int.*, 2018, **44**, 4685–4688.

44 B. Liu, L. Wang, H. Gu, H. Sun and H. V. Demir, *Adv. Opt. Mater.*, 2018, **6**, 1800220.

45 U. Kwon, B. Kim, D. C. Nguyen, J. Park, N. Y. Ha, S. Kim, S. H. Ko, S. Lee, D. Lee and H. J. Park, *Sci. Rep.*, 2016, **6**, 30759.

